Materials Today Chemistry 35 (2024) 101835

Contents lists available at ScienceDirect

Materials Today Chemistry

journal homepage: www.journals.elsevier.com/materials-today-chemistry/

Enhancing oxygen evolution functionality through anodization and nitridation of compositionally complex alloy

Luka Suhadolnik [a,b,*], Marjan Bele [b], Milutin Smiljanić [b], Goran Dražić [b], Lidija D. Rafailović [c], Daniela Neumüller [c], Martin Šala [d], Anja Logar [b,h], Nejc Hodnik [b,e], Miran Gaberšček [b], Janez Kovač [f], Urška Trstenjak [g], Tiziano Montini [a], Michele Melchionna [a,**], Paolo Fornasiero [a,***]

[a] Department of Chemical and Pharmaceutical Sciences, University of Trieste, Via L. Giorgieri 1, 34127, Trieste, Italy
[b] Department of Materials Chemistry, National Institute of Chemistry, Hajdrihova 19, SI-1000, Ljubljana, Slovenia
[c] Department of Materials Science, Chair of Materials Physics, University of Leoben, Jahnstrasse 12, 8700, Leoben, Austria
[d] Department of Analytical Chemistry, National Institute of Chemistry, Hajdrihova 19, SI-1000, Ljubljana, Slovenia
[e] Jožef Stefan International Postgraduate School, Jamova 39, SI-1000, Ljubljana, Slovenia
[f] Department of Surface Engineering, Jožef Stefan Institute, Jamova 39, SI-1000, Ljubljana, Slovenia
[g] Advanced Materials Department, Jožef Stefan Institute, Jamova 39, SI-1000, Ljubljana, Slovenia
[h] University of Nova Gorica, Vipavska 13, 5000 Nova Gorica, Slovenia

ARTICLE INFO

Keywords:
Anodic oxidation
Surface modification of alloys
Compositionally complex materials
Electrocatalysis
Oxygen evolution reaction

ABSTRACT

Compositionally complex materials (CCMs) have recently attracted great interest in electrocatalytic applications. To date, very few materials were systematically developed and tested due to the highly difficult preparation of high-surface-area CCMs. In this work, a surface of a compositionally complex FeCoNiCuZn alloy (CCA) was nitridated with subsequent anodization leading to morphological and compositional modifications. Notably, the electrochemical surface area and surface roughness as well as the electrocatalytic activity of the anodized material exhibit significant enhancement. Oxygen evolution reaction (OER) activity by the anodized CCN (CCN–AO) proceeds with remarkably small overpotential (233 mV) at 10 mA cm^{-2} in 1 M KOH. Experimental characterization indicates that the oxidation state of Co plays a critical role in the Fe–Co–Ni electrocatalyst. The developed approach and design strategy open up immense prospects in the preparation of a new, affordable, scalable and effective type of complex and high-performance electrocatalytic electrodes with tunable properties.

1. Introduction

Heterogeneous catalysis has a never-ending demand for improving catalytic activity and stability optimization. This is the main driving force for the continuous development of nanostructured materials with improved electrocatalytic properties for various applications (needs). Numerous electrocatalytic processes, and among these, the oxygen evolution reaction (OER) presents a special challenge [1] as it is a key reaction for several renewable energy technologies. Efficient OER catalysis is vital for the sustainable production of hydrogen via water electrolysis, which is seen as an integral part of future energy mixes, as it is able to store the energy produced by renewable sources and return it to the electricity grid when consumption exceeds production [2]. Current OER benchmark catalysts are based on precious metals, namely IrO_2 and RuO_2, which show the highest activity and durability. However, these materials have cost, scarcity, and durability limitations [3]. Therefore, alkaline electrolysis offers a promising alternative for sustainable and economically viable OER applications. Standard catalysts for the alkaline OER utilize materials such as nickel (Ni), cobalt (Co), or iron (Fe), either individually or in combination [4,5].

In recent years, high-entropy alloys (HEAs), high-entropy oxides (HEOs), and high-entropy ceramics (HECs) were introduced as an intriguing class of materials with versatile applicability, including electrocatalysis [6]. Such compositionally complex materials (CCMs)

* Corresponding author. Department of Chemical and Pharmaceutical Sciences, University of Trieste, Via L. Giorgieri 1, 34127, Trieste, Italy.
** Corresponding author.
*** Corresponding author.
E-mail addresses: luka.suhadolnik@units.it, luka.suhadolnik@ki.si (L. Suhadolnik), melchionnam@units.it (M. Melchionna), pfornasiero@units.it (P. Fornasiero).

https://doi.org/10.1016/j.mtchem.2023.101835
Received 30 September 2023; Received in revised form 15 November 2023; Accepted 28 November 2023
Available online 12 December 2023

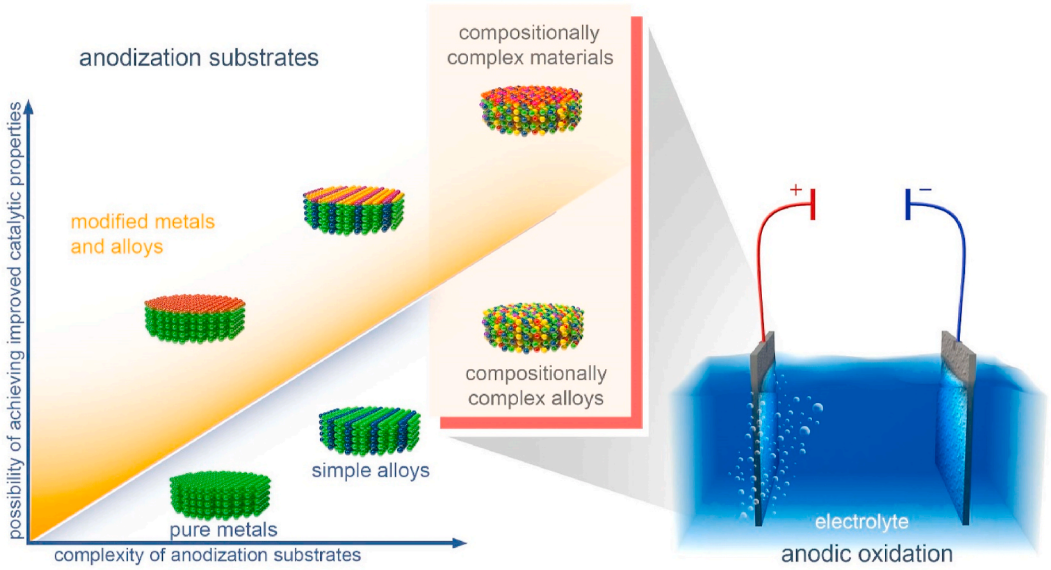

Fig. 1. The perspective of the present work into the state-of-the-art of anodization process. Materials in the colored regions of the left graph have never been investigated as anodization substrates. In this paper, we studied the anodization of CCA and CCN in order to prepare compositionally complex oxide (CCO).

contain at least five elements and no single dominant element and were first introduced as HEAs in 2004 [7,8]. Interest in these materials initially focused on overcoming the mechanical properties of traditional alloys [9]. However, due to their manifold functional and structural properties, HEAs today draw great attention in many fields of materials science, in particular for electrocatalytic applications [10,11].

The concept is to take advantage of the randomly distributed atoms of various metals in a defined crystalline structure of HEA. A HEA's active surface is made up of many different surface sites arising from the numerous combinations of nearest neighboring atoms. This results in a plethora of catalytic properties due to the synergistic interactions between different transition metals that are in contact [10]. However, despite some intriguing properties, many HEAs exhibit low specific surface area which compromises suitability for electrocatalytic applications [7,12,13]. In fact, high surface area is in practice mandatory for high activity in heterogenous catalysts, and thus crucial for the design of high-performance electrocatalysts. Moreover, alongside surface area considerations, the choice of metals and their potential interactions and synergies, such as tuning electronic states through orbital mixing, play an important role in the development of efficient catalytic systems [14].

To overcome the issue of low surface area, a synthesis of nanoporous HEA covered with high entropy (oxy)hydroxides was reported in 2019 [15]. It was composed of Al, Ni, Co, Fe, and/or Mo, Nb or Cr and used as an OER catalyst in alkaline media. These new materials highlighted the importance of incorporating five metal elements in one single-phase nanostructure. Recent studies on high entropy material (HEM) catalysts for electrocatalytic applications revealed that CCMs are very promising candidates for high-performance heterogeneous catalysis [15–20].

Due to the lack of simple synthetic methods that can give access to heterogeneous materials closely interconnected at the nanoscale, only a few different combinations of nanostructured non-noble metal CCMs have been investigated. While there are numerous methods for preparing powder single-phase solid solution HEA nanoparticles (NPs), all of them are complex and excessively time-consuming. Furthermore, application in electrocatalysis implies that the nanoparticulate HEAs must be immobilized on a conductive support. This can be accomplished using the drop-casting method [19], electrochemical deposition [21], or more complex approaches such as sputtering HEA thin films [22,23]. The advantage of these approaches is that the HEAs surface can be more easily modified to design a nanostructured compositionally complex surface. However, the majority of such HEAs still exhibit rather low surface area and potential conductivity problems and are therefore currently for the most part unreliable for practical electrocatalytic applications without further optimization.

Anodic oxidation (AO) is a relatively simple synthetic process for modifying metals and alloys, producing strongly attached, highly porous and even regularly ordered structures that can serve as electrodes without further processing. As is known from the anodization of pure metals and simple commercial alloys, porosity is controlled by the presence of fluorine in the anodization electrolyte [24,25]. AO has been recently applied for the development of a diverse spectra of materials with varying morphologies, including nanostructured films of nickel oxide [26], iron oxide [27], titanium oxide [28], cobalt oxide [29], copper oxide [30], zinc oxide [31] and other transition metal elements that are the most promising non-noble electrocatalysts [32]. Anodization processing conditions (anodization voltage and time as well as electrolyte temperature and composition) for the preparation of these materials frequently differ, meaning that the requirements for optimal AO-derived materials are more stringent than for pure metals. Nonetheless, published research on the anodization of various simple alloys [33–35] demonstrates that complex materials can also be anodized. Based on these considerations, anodization of CCMs composed of transition-metal elements (Fig. 1) has the potential to become a highly convenient strategy to prepare complex multicomponent nanostructured films, strongly attached to support with almost unlimited material combinations.

In the present work, we focus on the AO of FeCoNiCuZn alloy which was critically modified using nitridation under gaseous ammonia flow prior to the AO. As a result of the CCM-tuned structure, we achieved an OER performance that stands among the best-ever electrocatalysts based on non-noble metals.

Our new synthetic methodology offers a number of relevant advantages: i) the CCM is strongly immobilized on the conductive support; ii) the surface area is greatly enhanced as compared to CCMs prepared with other methods; iii) the hierarchical structure of the CCM evolves with the formation of controlled pore distributions. Apart from the significant OER performance arising from the tailored structure, this work presents a versatile synthetic method for developing new AO-based CCMs with optimized properties for other specific electrocatalytic processes.

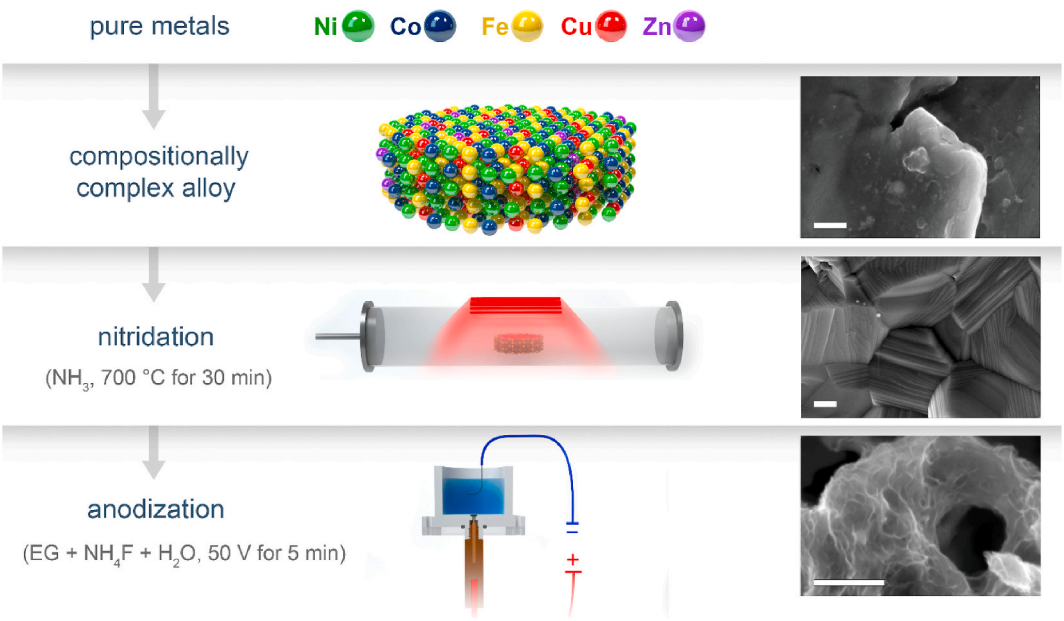

Fig. 2. Scheme of the new methodology for the synthesis of immobilized multicomponent nanostructured films using anodic oxidation of nitridated compositionally complex alloys. On the right, SEM micrographs show realistic top surface morphology during each synthesis step. Scale bars sizes represent 200 nm.

2. Experimental

Preparation of compositionally complex alloy: Compositionally complex bulk materials (FeCoNiCuZn) were produced by arc melting (Edmund Bühler GmbH, Germany) of the pure elements. The Fe, Co, Ni, Cu, and Zn granules had a purity of 99.99 % and were purchased from HMW Hauner GmbH & Co. KG in Germany. The preparation was carried out in a Ti-getter Ar atmosphere. The ingots were heated 5 times above the liquidus temperature and turned after each melting and cooling/crystallization cycle to ensure homogeneous material preparation. The obtained ingot was cut into 1 mm thick pieces, and then 4 mm diameter cylinders were punched.

Nitridation of compositionally complex alloy: Nitridation was conducted at 700 °C for 30 min in a constant ammonia flow of 100 cm^3 min^{-1} at 1 atm pressure, with heating and cooling rates of 10 °C min^{-1}.

Anodization of compositionally complex materials: Compositionally complex samples were subjected to anodization in a custom-developed electrochemical cell (Fig. S1) using similar anodization parameters as reported by Suhadolnik et al. [36] Samples were first inserted into a custom-made Teflon holder which was sealed into the bottom of the cell with an o-ring. The entire top surface of a sample was exposed to the always freshly prepared electrolyte.

The anodization voltage was adjusted within the range of 40 V–60 V, while the anodization duration spanned from 1 min to 20 min. The same Teflon holder that was used for anodic oxidation was later mounted on a rotator for rotating disk electrode electrochemical measurements.

2.1. Materials characterization techniques

SEM and SEM–EDXS analysis: The surface morphology of all samples was examined under the conditions previously reported by Suhadolnik et al. [36].

XRD: All samples underwent characterization via X-ray diffraction under the conditions outlined by Suhadolnik et al. [36] The phase identification was performed with the X'Pert HighScore Plus program using the International Centre for Diffraction Data (ICDD) PDF-4+ 2021 database [37].

XPS: The surface composition of compositionally complex samples was analyzed with X-ray photoelectron spectroscopy (XPS) under the conditions previously reported by Suhadolnik et al. [36] The accuracy of binding energy was ±0.5 eV. XPS spectra were elaborated with Multipak software, version 9.9. XPS spectra Fe 2p, Ni 2p and Co 2p were used for quantification of surface composition and identification of oxidation states. We should note that in these spectral regions, many overlaps of the Auger MNN spectra and metallic 2p spectra are present due to similar electronic structures of the Fe, Ni and Co. This complicates and limits identification of oxidation states and quantification of surface composition. The relative error of concentrations of surface composition determined by XPS is about 30 % of the reported concentration.

TEM techniques: TEM imaging was performed in the same way as previously reported by Suhadolnik et al. [36].

Confocal laser scanning microscopy (CLSM): Surface topology and roughness of the samples were analyzed using laser scanning confocal microscopy, specifically an Olympus LEXT OLS4000 3D laser microscope, which provided optical images with depth selectivity. Evaluation of the data was done with Gwyddion free software [38].

Atomic force microscopy (AFM): AFM (Dimension Icon with ScanAsyst, Bruker) in tapping mode was used to capture topography images. AFM topography analysis was done with a Bruker Dimension Icon atomic force microscope employing a TESPA-V2 etched silicon probe (Bruker). Gwyddion, a free software, was used to correct the images [38].

ICP-MS of KOH electrolyte during stability test: Samples collected at different times during electrocatalytic stability test were analyzed using ICP-MS after appropriate dilution and acidification. For sample dilution and preparation of standards, ultrapure water (MilliQ, Millipore) and ultrapure acids (HNO_3, Merck, Suprapur) were used. Standards were prepared in-house by dilution of certified, traceable, inductively coupled plasma-(ICP) grade single-element standards (Merck Certipur). An Agilent quadrupole ICP-MS instrument (Agilent 7900, Agilent Technologies, Santa Clara, CA), equipped with a MicroMist glass concentric nebuliser, and Peltier-cooled, Scott-type spray chamber was used for the measurement.

Electrochemical Measurements: All electrochemical measurements were conducted at ambient temperature within a single-compartment electrochemical cell, featuring a three-electrode configuration. All the prepared materials were inserted into a custom-made Teflon holder (the same as was used for anodization) and used as a working electrode. The reference electrode employed was a HydroFlex reversible hydrogen electrode (RHE, Gaskatel GmbH), while a glassy carbon rod served as the

Table 1
Chemical composition (at.%) of CCA and CCN determined with XPS and SEM–EDXS for both samples and additionally STEM–EDXS for CCA. Carbon was not taken into account.

COMPOSITIONALLY COMPLEX ALLOY (CCA)							
Analysis	Fe	Co	Ni	Cu	Zn	O	N
XPS	9.0	10.1	6.5			72.6	1.8
SEM–EDXS	24.0	24.3	23.9	13.2	4.9	9.6	
STEM–EDXS	33.7	34.1	32.2				
COMPOSITIONALLY COMPLEX NITRIDE (CCN)							
XPS	9.2	14.2	4.9			55.4	16.3
SEM–EDXS	25.2	21.3	24.2	13.1	0.8	1.6	14.6

counter electrode. The potential was regulated using a potentiostat (SP-300, Biologic). For activation and specific surface area determination, the supporting electrolyte was N_2-saturated 1 M KOH (99.995 %, Suprapur, Merck) aqueous solution; whereas, for linear sweep voltammetry (LSV) measurements, O_2-saturated 1 M KOH was utilized. Activation entailed cyclic voltammetry (CV) cycling between 0.25 and 0.35 V vs RHE for 100 cycles at a scan rate of 300 mV s^{-1} to attain a stable cyclic voltammogram. Following this pretreatment, the OER activity was assessed through LSV at a scan rate of 2 mV s^{-1}. The resistance of the electrolyte was recorded by electrochemical impedance spectroscopy (EIS) before each OER activity measurement and the iR compensation of 85 % was applied. The overpotential (η) at 10 and 100 mA cm^{-2} was calculated using the equation $\eta = E$ (at 10 or 100 mA cm^{-2}) – 1.23 V.

Determination of double layer capacitance (C_{dl}) of all catalysts was done electrochemically. The C_{dl} of the catalysts was determined by measuring the capacitive current associated with double-layer charging from the scan-rate dependence of cyclic voltammetry stripping. CV curves were measured in the potential window from 0.25 to 0.35 V versus RHE at scan rates of 20, 50, 100, 200, and 300 mV s^{-1}. The C_{dl} was estimated by plotting the $\Delta J = J_a - J_c$ at 0.3 V vs RHE against the scan rate, the linear slope is twice of C_{dl}.

IrO_x benchmark material (Premion, Alfa Aesar) was measured in a three-electrode configuration cell with a thin film of IrO_x powder deposited on a glassy carbon RDE, which was used as a working electrode and HydroFlex reversible hydrogen electrode (Gaskatel GmbH) and carbon rod as reference and counter electrodes, respectively. Thin films were prepared by drop casting 20 μL of IrO_x ink, prepared by dispersion of nanoparticles in Milli-Q water (18.2 Ω cm). Additionally, 5 % Nafion stock solution (Aldrich) was added to the ink, so that the amount of Nafion was 25 wt% of the solid content in the suspension. The electrochemical protocol consisted of 20 cycles (50 mV s^{-1}) between 0.05 and 1.45 V and subsequent activity measurement by recording an LSV from 1.2 to 1.6 V with a scan rate of 2 mV s^{-1}. Both activation and activity were measured in an Ar-saturated electrolyte. Afterward, activity measurement was repeated also in O_2 atmosphere.

3. Results and discussion

3.1. Characterization of synthetic intermediates of compositionally complex catalyst preparation

The new catalyst was prepared through a three-step procedure consisting of i) the preparation of a CCA, ii) the annealing of the CCA in an NH_3 atmosphere, and iii) the anodization of the nitridated alloy. Fig. 2 depicts a schematic representation of the preparation.

CCA in bulk form was prepared from equimolar amounts of Fe, Co, and Ni, as well as lower amounts of Cu and Zn. A detailed description of the CCA synthesis can be found in the experimental section. Briefly, pure elements were arc melted in a Ti-getter Ar atmosphere and heated 5 times above the melting temperature to make the ingots homogeneous. According to SEM (Figs. S2a and b) and AFM (Fig. S2c), the top surface morphology of CCA is a relatively uniform and smooth disc. The surface roughness of the CCA sample represented by root mean square (RMS) value is 16 ± 2 nm. The same roughness parameter obtained with confocal laser scanning microscopy (CLSM) at lower magnification (100 ×) was determined to be 3.2 μm (Fig. S2c). SEM–EDXS mapping (Fig. S3) and XRD analysis (Fig. S4a) reveal a bulk equimolar $Fe_{0.333}Co_{0.334}Ni_{0.333}$ phase as well as app. 18 at.% of $Cu_{0.76}Zn_{0.24}$ phase in the $Fe_{0.333}Co_{0.334}Ni_{0.333}$ matrix (Table 1). The $Cu_{0.76}Zn_{0.24}$ phase with diffraction peaks (●) (PDF 04-004-8062) is a solid solution of Zn in α-Cu [39] that was intentionally added to the alloy to cause the formation of larger pores via dealloying during the AO process. The diffraction peaks (◆) are related to cubic structure and Fm-3m space group of $Fe_{0.333}Co_{0.334}Ni_{0.333}$ (PDF 04-024-3627). XPS analysis shows Fe, Ni, Co, O, and C in the surface oxide layer of CCA (Fig. S5). Cu and Zn were not detected possibly because of their low concentrations in upper layers. The presence of metallic oxide peaks and relatively strong metallic peaks of Fe, Ni, and Co is the main feature of Ni, Fe, and Co spectra. This is explained as a 3–5 nm thick native oxide Fe–Ni–Co layer covering the metallic Fe–Ni–Co matrix.

STEM analysis of the lamella prepared in cross-section orientation revealed a relatively rough surface of the complex alloy. The substrate alloy consists of tens of microns large grains. Selected area electron diffraction (SAED) of one of such grains is shown in Fig. S6b. EDXS mappings (Fig. S6c) show that Fe, Ni and Co are homogeneously distributed in the substrate grain and oxide film.

Nitridation of CCA in NH_3 at 700 °C for 30 min results in faceted crystal planes of compositionally complex nitride (CCN) as determined with SEM analysis (Figs. S7a and b). The faceted morphology of CCN is dominated by the mixed metal nitride phase (○) with a homogeneously distributed cubic Pm-3m crystallographic structure, according to XRD analysis (Fig. S4b) and elemental SEM-EDXS mapping (Fig. S8). The diffraction peaks appear relatively narrow, in agreement with the SEM analysis revealing the presence of large crystallites. Because of the relatively thick nitridated film, the diffraction peaks corresponding to the CCA support are barely visible. Due to the sublimation of most Zn during high-temperature annealing [40], the $Cu_{0.76}Zn_{0.24}$ phase is no longer present, while some peaks assigned to metallic Cu (□) are observed. The surface roughness of the CCA has increased from 16 ± 2 nm to 83 ± 22 nm for the CCN material, as determined by AFM analysis (Fig. S7c).

XPS analysis of the CCN sample (Fig. S9) shows that the surface consists of a thin layer of mixed oxides with thickness in the range of 3–5 nm and the nitrides/oxynitrides, as evidenced by N 1s spectrum with the peaks at 397.5 eV and 399 eV. The high-resolution XPS spectra of Fe 2p and Co 2p are similar to that of the CCA sample. After nitridation, the shape of the Ni 2p spectrum has changed. Concerning the oxidized Ni(2+/3+), a peak at 853.1 eV associated with Ni(0) and/or Ni-nitride/oxynitride formation is increased. These findings indicate that the top surface of the CCA has been transformed into a homogeneous CCN phase with metallic copper inclusions.

Table 1 shows the chemical composition of CCA and CCN samples. Aside from the sublimation of Zn and the replacement of the majority of oxygen with nitrogen, the relative amounts of the three main elements have changed slightly. Notably, the Co amount is decreased according to SEM-EDXS analysis; however, it is increased by XPS analysis, which examines the top-most 3–5 nm.

3.2. Anodic oxidation of CCM for the preparation of final catalyst

It is known that electrolyte composition, as well as anodization potential and time, allow for fine-tuning of anodized materials' morphology, structure, and functional properties, and that different metals typically require anodization in different anodization electrolytes [27,29,41]. The choice of the solvent/electrolyte is an important parameter, which must consider the type of metals to be anodized [30, 42,43]. [44–46] Additionally, the concentration and type of salt

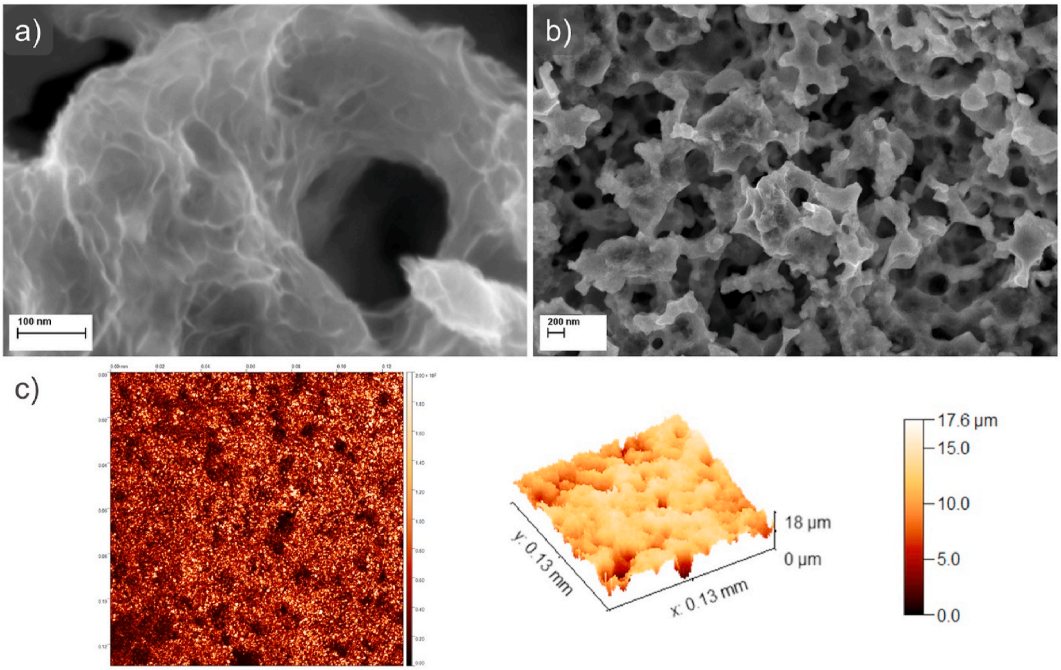

Fig. 3. SEM and CLSM analysis of CCN–AO catalyst anodized at 50 V for 5 min. a) and b) top surface morphology and c) CLSM image and corresponding profile.

(fluoride vs. other) strongly influence the anodization process. Most common anodization potentials range between 40 and 60 V, so that a potential of 50 V was chosen for the AO process. We used a solution of ethylene glycol, ammonium fluoride and water as the electrolyte as this is the typical composition used for the anodization of Fe, Co and Ni [27, 29]. However, such conditions are not compatible with copper and zinc (usually anodized in aqueous electrolytes and at potentials lower than 30 V), which are removed during the AO, but they are still essential to

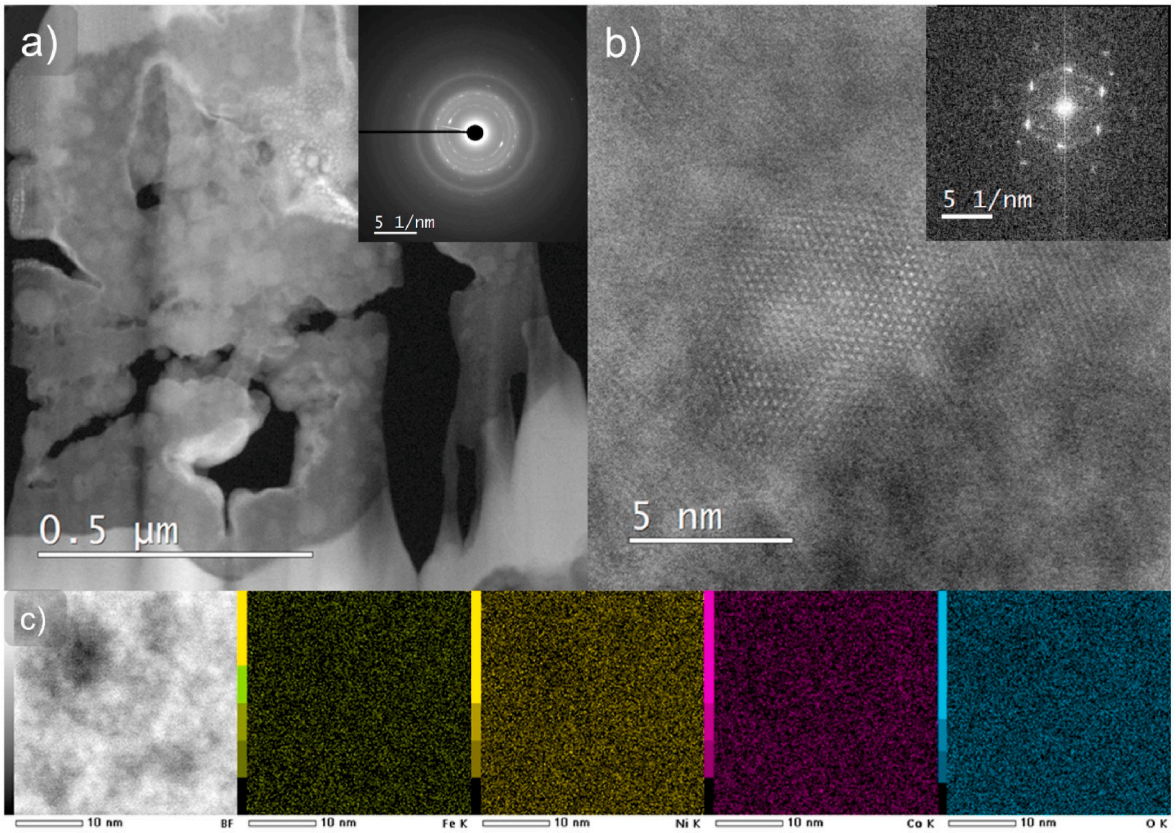

Fig. 4. STEM characterization of CCN–AO catalyst. a) HAADF-STEM of oxide film at low magnification with the SAED as an inset, b) high-resolution HAADF image of the nanoparticle in the oxide film with a FFT as an inset and c) STEM–EDXS analysis of cross-sectioned FIB lamella of CCN–AO catalyst anodized at 50 V for 5 min.

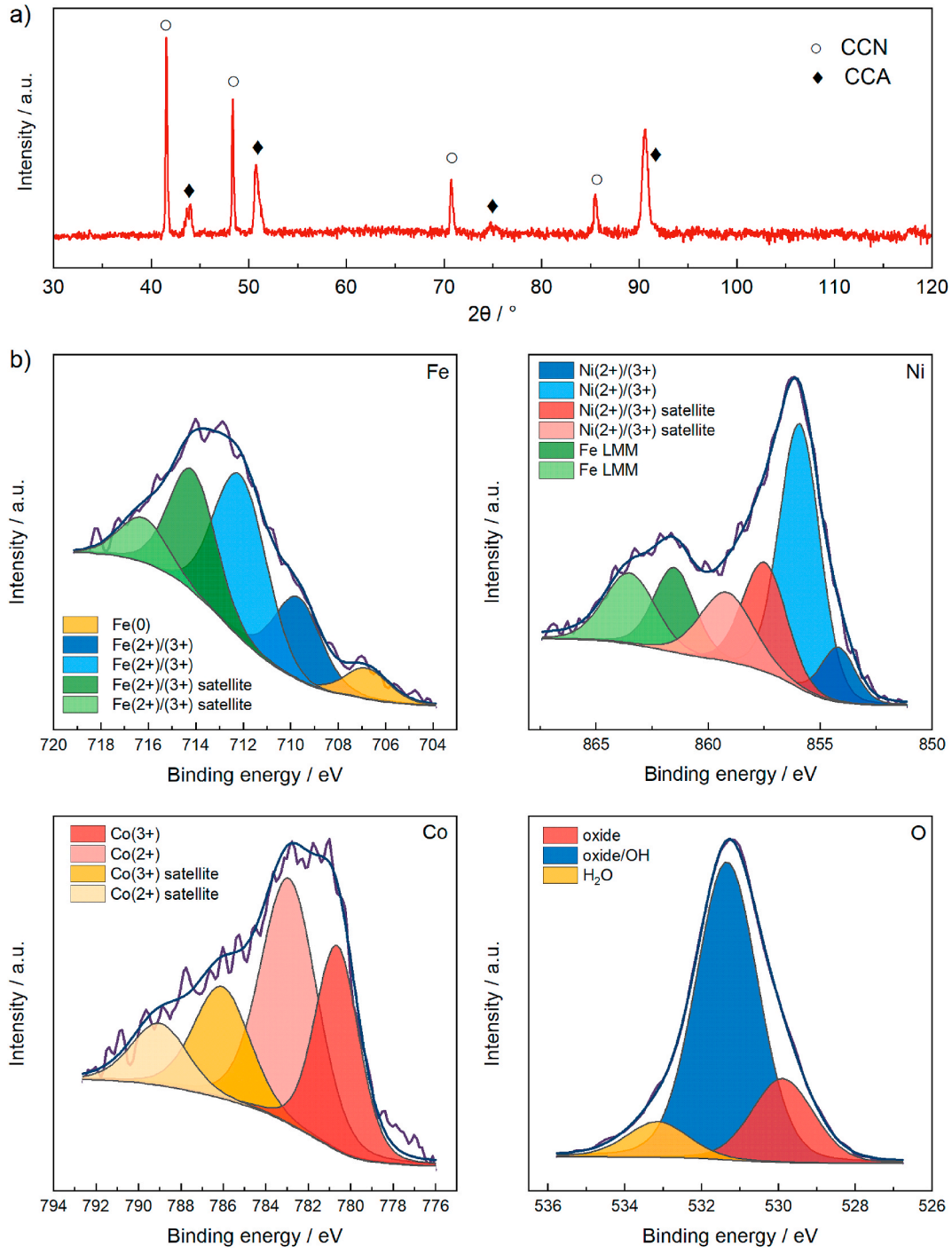

Fig. 5. XRD and XPS analysis of CCN–AO catalyst. a) XRD diffractogram showing peaks (◆) related to CCA and peaks (○) related to CCN and b) XPS analysis showing Fe 2p, Ni 2p, Co 2p, and O 1s spectra from the surface. The standard cards of XRD diffractogram in a) are included in Fig. S4.

introduce controlled porosity. It is known that the hierarchical organization of pores in the catalyst film improves its performance [47–49] due to enhanced mass transport, the accessibility of active sites and better conductivity due to interconnectivity. More specifically, the removal of Cu and Zn pockets (templates) during nitridation and anodization resulted in larger pores (>100 nm) for fast ionic and electronic paths, whereas fluoride ion etching of the CCA and CCN form smaller pores (<20 nm) interconnected with the larger porous architecture.

To assess the significance of the nitridation step, we evaluated the performance of a reference catalyst where the AO process was carried out directly on the CCA (CCA-AO). Notably, we observed that the current density time curve for CCA-AO considerably differs from that of CCN-AO (Fig. S10). While the current of the non-nitrated sample (CCA) decreases quickly after the start of the anodization, the CCN anodization current remains constant or even slightly increases after a few minutes at 60 V. Only Co anodization exhibits a similar anodization current density behavior [29]. However, we note that the current range observed for Co is much lower than the one of our CCM materials, which is close to 200 mA cm^{-2} at 60 V. The increased surface roughness (Fig. S2c and Fig. S7c) of the CCN thin film is responsible for the higher total charge passed during the CCN anodization compared to CCA anodization.

Table 2
Chemical composition of anodized CCN determined with XPS, SEM–EDXS, and STEM–EDXS. F is also present; however, it was removed from table so that it is easier to compare samples.

Sample name	Fe	Co	Ni	O	N
SEM–EDXS	14.6	11.5	15.0	57.2	1.7
STEM–EDXS	11.0	10.0	20.0	59.0	
XPS	7.8	6.8	11.1	74.3	

Anodization potential also influences anodization current density, which increases as anodization potential increases (Fig. S11). We found that anodizing CCN results in homogeneous top surface morphology (Fig. 3 and Fig. S12), whereas anodized non-nitrated sample resulted in two morphologically and compositionally distinct regions (Fig. S13).

The following two sections provide a detailed description of anodized CCN properties.

3.3. Characterization of final catalyst

The most efficient anodically oxidized compositionally complex nitride (CCN–AO) catalyst was prepared with nitridation of CCA at 700 °C for 30 min at the NH_3 flow rate of 100 cm^3 min^{-1}, followed by 5 min of anodization in fresh electrolyte at 50 V. Several techniques were used to characterize the catalyst.

The top surface morphology of CCN–AO was firstly investigated by SEM and CLSM. AFM could not be used on this sample since its surface roughness exceeds the limits of the measurement method. As shown in Fig. 3, CCN–AO exhibits highly porous, high surface-area morphology. The RMS value for the surface roughness of the CCN–AO sample is 2.1 ± 0.5 μm. Additional SEM micrographs at various magnifications show that the film is highly homogeneous with regions made of larger pores (Fig. S14). The latter were formed as a result of the removal of Cu and Zn during nitridation and anodization and are important for the film's hierarchical porous morphology. Such a pore organization increases the exposed active sites and the contact area with the electrolyte, resulting in enhanced catalytic performance.

STEM structural analysis of CCN–AO lamella (Fig. 4) reveals that the immobilized catalyst is app. 1 μm thick, with pores of varying sizes present throughout the entire film thickness. The atomic resolution analysis (Fig. 4b) confirms that the film is composed of oxide nanoparticles with a size of about 5 nm. Selected area electron diffraction (SAED) pattern shows the combination of many possible phases. Although anodization typically leads to amorphous or poorly crystallized nanostructured films, the anodized CCN prepared in this study exhibits extended crystalline domains, as determined by TEM diffraction. The STEM–EDXS mapping reveals a partially homogeneous distribution of all the Fe, Ni, and Co. According to electron energy loss spectroscopy (EELS) analysis Ni and Co are close to 2+ oxidation state, whereas Fe is close to the 3+ state. Meanwhile, CCN–AO anodized at 60 V for 5 min also exhibits a homogeneous elemental distribution in a much thinner (app. 400 nm) porous film (Fig. S15).

XRD analysis of CCN-AO (Fig. 5a) revealed that the anodized film could not be detected in the diffractogram due to tiny oxide nanocrystallites and/or the amorphous nature of the portion of the film. As a result, only the CCN (○) and CCA (◆) peaks are visible, with the CCA peaks being more intense due to CCN etching during the anodization process.

The survey XPS spectra of CCN-AO (Fig. 5b) reveal the presence of Fe, Ni, Co, and O elements on the surface. A mixed oxide layer is present as well as traces of F. The most intense Fe $2p_{3/2}$ peak is at 712.3 eV, the most intense Ni $2p_{3/2}$ peak is at 855.9 eV, and the most intense Co $2p_{3/2}$ peak is at 782.9 eV. Oxidation states present in the oxide layer are Fe (2+/3+), Ni(2+/3+) and Co(2+/3+). The oxygen spectrum O 1s has three peaks: 529.8 eV (oxide), 531.3 eV (oxide and OH), and 532.3 eV (oxygen) (adsorbed H_2O).

Table 2 shows the chemical composition of the CCN–AO catalyst as determined by SEM–EDXS, STEM–EDXS, and XPS. XPS elemental composition was measured at the surface. Different analyses yield different results, which is due to the different analyzed volumes. XPS and STEM–EDXS show no N which is observed in SEM–EDXS analysis. A much more pronounced difference is that there is a lower percentage of Fe at the surface (XPS measurement) than in the film and bulk CCA below the film (SEM–EDXS measurement). Furthermore, elemental SEM–EDXS mapping (Fig. S16) reveals a uniform distribution of all elements as well as the presence of some Cu that is not in the film but in the CCA substrate.

3.4. OER electrocatalytic evaluation

Multiple synthesis processes and parameters were screened to evaluate the electrocatalytic performance of CCA and other catalysts derived from the initial alloy to obtain the optimized CCN–AO catalyst. Based on our findings, the following rationale can be developed. First, due to their low specific surface area, the synthetic intermediates (CCA and CCN) of CCN–AO have very low electrocatalytic activity (Fig. S17). Second, our experiments show that direct anodization of CCA results in significantly

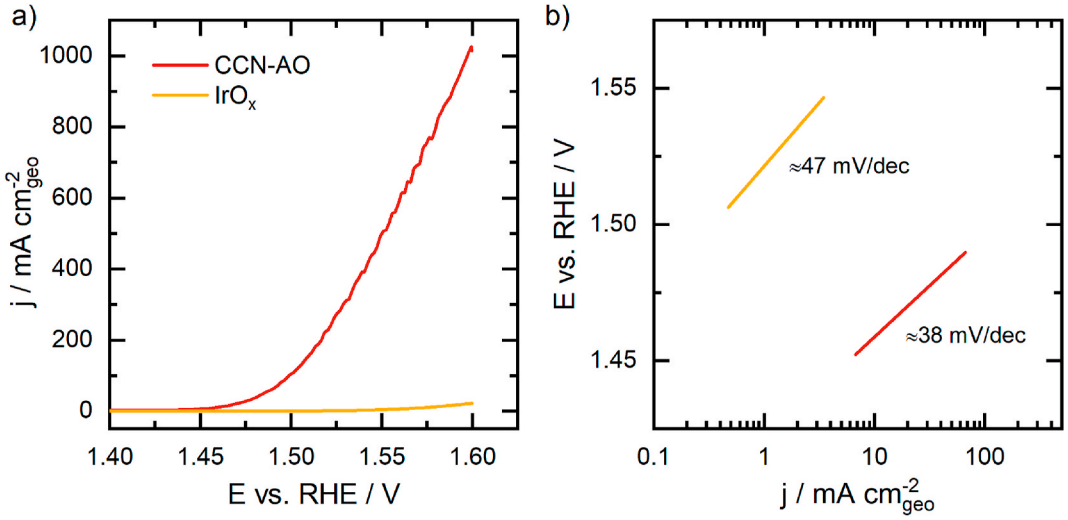

Fig. 6. A) OER performance of CCN–AO catalyst and IrO_x benchmark. The OER polarization curves are normalized per geometric surface area. b) Tafel plot of OER polarization curves (constructed from a). Activity was determined in 1 M KOH (*Titripur*, Merck) electrolyte.

Table 3
Chemical composition of the CCN–AO before and after electrocatalytic activity measurement as well as after electrocatalytic stability measurement. The composition was determined with SEM–EDXS and XPS and is shown in at.%. 3.8 at.% F is also present in CCN–AO; however, it was removed from table so that it is easier to compare samples.

AS PREPARED CCN–AO					
Sample name	Fe	Co	Ni	O	N
XPS	7.8	6.8	11.1	74.3	
SEM–EDXS	14.6	11.5	15.0	57.2	1.7
AFTER EC ACTIVITY					
XPS	5.8	5.0	12.6	76.6	0
SEM–EDXS	14.6	11.4	16.0	56.8	1.2
AFTER EC STABILITY (24 h at 10 mA cm^{-2})					
XPS	4.4	5.2	7.1	83.3	
SEM–EDXS	10.8	10.9	16.7	61.7	

lower OER activity as compared to that of the CCA which is nitridated prior to anodization (Fig. S18). The nitridation step significantly alters the alloy composition (sublimation of Zn, Table 1), structure (alloy is transformed into the CCN, Fig. S4), and morphology (faceted crystal planes of the nitride, Figs. S7a and b compared to Figs. S2a and b). Third, anodization time (Fig. S19) has a significant impact on OER activity.

Based on these findings, the catalyst with the highest OER activity was analyzed in depth. The electrocatalytic performance of CCN–AO (Fig. 6) was determined by Linear sweep voltammetry (LSV) measurements in 1 M KOH (Potassium hydroxide solution, *Titripur*, Merck) actively purged with O_2 and recorded at a scan rate of 2 mV s^{-1}. Purging with O_2 is advised to maintain the O_2/H_2O equilibrium at 1.23 V vs RHE, whereas a low scan rate is required to minimize the frequently observed high redox peaks of common catalysts for alkaline OER at a potential slightly above 1.23 V vs RHE [50]. Fig. 6 compares the performance of an immobilized thin-film CCN–AO catalyst to that of a commercial IrO_x deposited on a glassy carbon electrode (GCE). The app. 1 μm-thick CCN–AO film with double layer capacitance of app. 1.5 mF cm^{-2} results in an overpotential of 233 mV to achieve a current density of 10 mA cm^{-2} which is 111 mV lower than the one of the IrO_x benchmark with an overpotential of 344 mV. Furthermore, the observed Tafel slope of the CCN–AO was app. 38 mV dec^{-1} whereas the one for the IrO_x benchmark was 47 mV dec^{-1} indicating that the CCN–AO has much faster OER kinetics. For commercial applications, the overpotential value at 100 mA cm^{-2} or higher, which is 270 mV for our CCN–AO catalyst, should also be reported. We note that commercial alkaline electrolyzers operate at current densities from 100 to 400 mA cm^{-2} [51].

The CCN–AO activity and Tafel slope value are comparable to the activity of the best-reported catalysts (G-FeCoW on GCE) thus far, which had an overpotential of 223 mV to reach 10 mA cm^{-2} and a Tafel slope of 37 mV dec^{-1} [52]. Table S1 compiles the best-performing non-noble alkaline OER electrocatalysts. However, the catalyst support material is the primary factor preventing direct comparison of published research. Even though GCE support is commonly used, the measured double-layer capacitance varies significantly among catalyst films, ranging from less than 0.1 mF cm^{-2} to nearly 150 mF cm^{-2} on the same type of support (GCE) [53,54]. Catalysts deposited on Ni foam, carbon cloth, or another high surface area substrate have a significantly lower OER overpotential [52,54] making a direct comparison with flat catalytic electrode surfaces of limited utility.

The impedance spectra of the CCN–AO were measured and compared with the typical spectra of the IrO_x on the GCE benchmark (Fig. S20). Both materials were measured at 1.5 V and 1.55 V vs. RHE, i.e., within the window recommended in our recent article [55], which represents a good compromise between stability of the spectra and activity of the catalyst. It can be seen that for both potentials, the arc corresponding to the final catalyst is much smaller than the arc corresponding to the IrO_x benchmark. A detailed analysis of the spectra using the equivalent physical circuit in Figure S19 [55,56] shows that the total resistance ($R_a + R_{ct}$) at 1.5 V and 1.55 V versus RHE is 140 times and 15 times smaller, respectively, in the case of the CCN–AO than in the case of the IrO_x reference. This means that a similar difference in the slope of the two polarization curves at the respective potentials is also to be expected because the total resistance is supposed to exactly correspond to the slope in the ideal measurement.

SEM, SEM–EDXS, and XPS were used to analyze the catalyst after the electrochemical activity test. The top surface morphology (Figs. S21a and b) as well as the composition determined by SEM-EDXS (Table 3) are comparable to the catalyst before electrochemical analysis. The electrochemically analyzed sample's XPS spectra (Figs. S21c–f) are similar to the analysis of the CCN–AO sample, with some new features related to the chemistry of the Co atoms. The most intense Fe $2p_{3/2}$ peak is located at 711.4 eV, the Ni $2p_{3/2}$ peak is located at 855.6 eV, and the Co $2p_{3/2}$ peak is located at 780.7 eV. The oxide layer contains the oxidation states Fe (2+/3+) and Ni(2+/3+). The Co $2p_{3/2}$ spectrum was significantly altered when compared to the CCN–AO sample, indicating that the electrochemical activation has a great impact on the Co atoms' chemical status. The main Co $2p_{3/2}$ peak at 780.7 eV is assigned to the Co(3+) state. This is confirmed by lowering the peak at 783 eV, which is typical

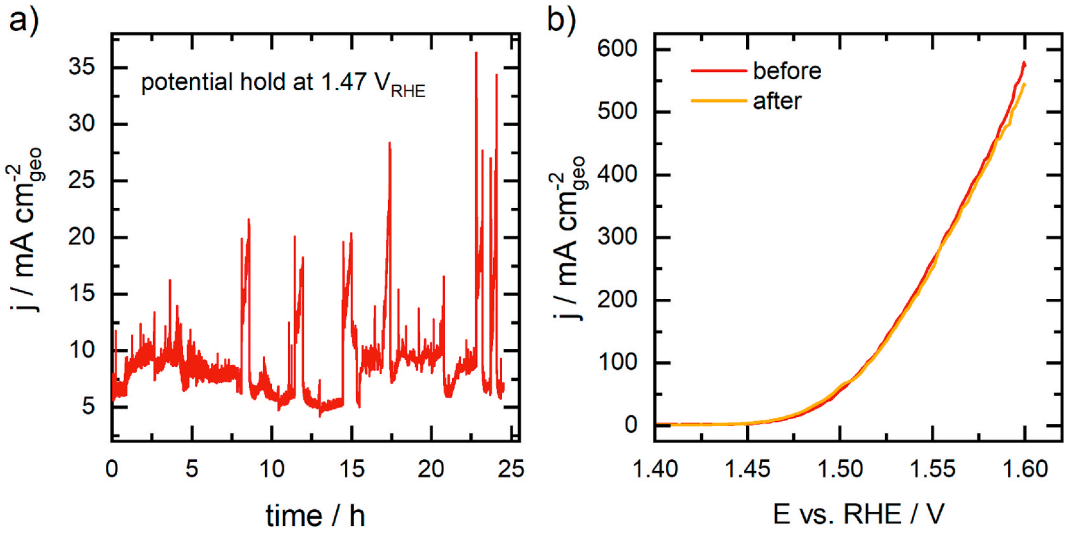

Fig. 7. Stability of CCN–AO catalyst. a) Chronoamperometric stability test of CCN–AO at 10 mA cm^{-2} for 24 h in 1 M KOH (99.995 %, Suprapur, Merck). b) OER electrocatalytic activity before and after the stability test.

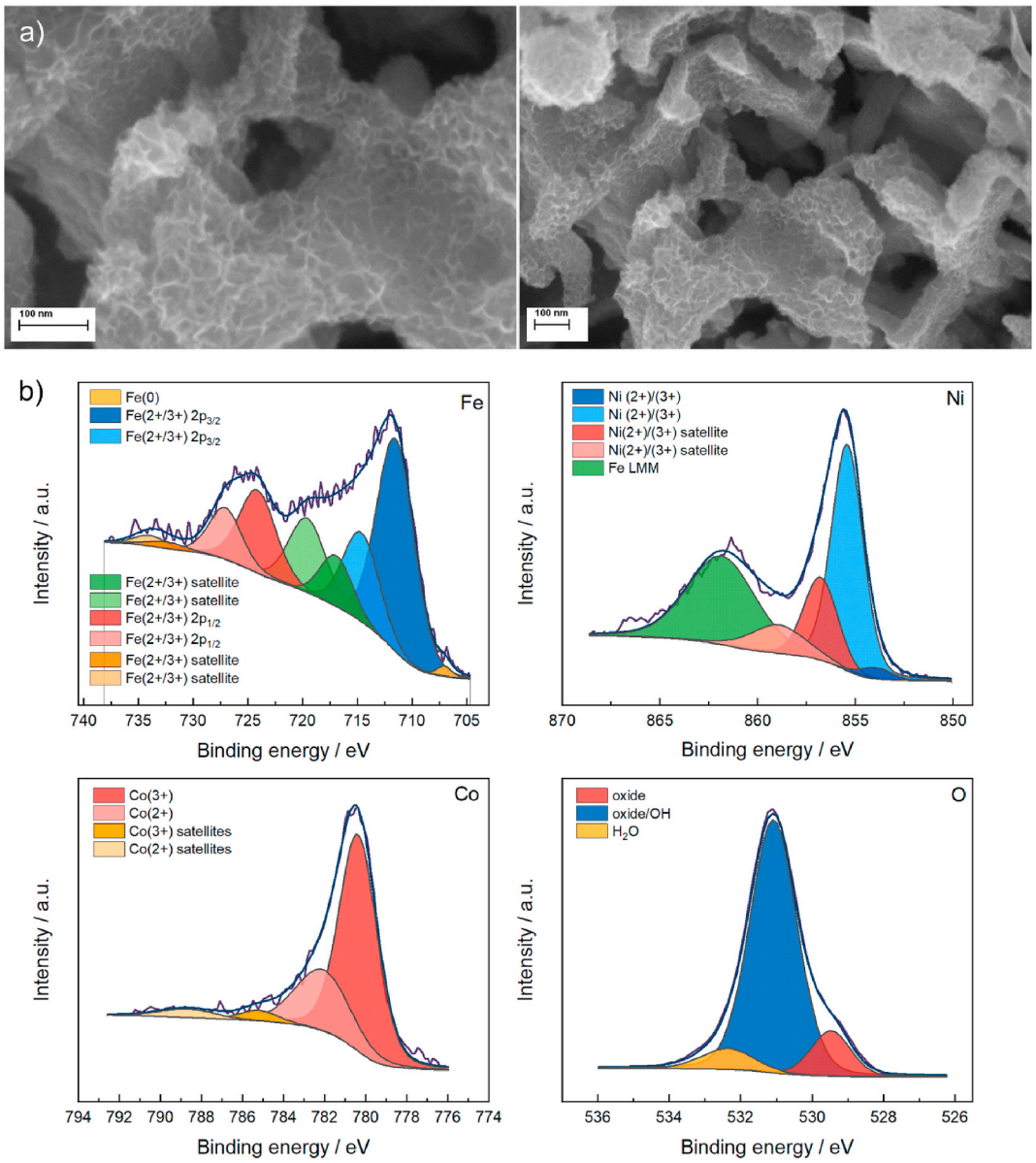

Fig. 8. SEM and XPS characterization of CCN–AO catalyst after the stability test. SEM (a), and XPS spectra (b) of the sample after the stability test. Fe 2p, Ni 2p, Co 2p, O 1s spectra are shown.

of pure Co(2+) states [57,58]. It is reported in the literature that incorporation of Co(3+) in the NiFe–based catalyst reduces the OER overpotential [59] which is confirmed in our study since we observed greatly increased catalyst activity during the electrochemical activation step which caused changes in the XPS spectra of Co (comparison of Fig. 5b and Figs. S21c–f). This indicates that the Co(3+) oxidation states play an important role in the OER reaction.

Durability of the CCN-AO catalyst was investigated to further investigate its OER performance (Fig. 7). Chronoamperometry (CA) was used to test the stability of the CCN–AO catalyst (Fig. 7a). Experiments were performed in high purity KOH (99.995 %, *Suprapur*, Merck), to prevent any possible contamination of the catalyst with impurities, as recently cautioned by the electrocatalysis community [60,61]. To minimize the effect of the excessive accumulation of O_2 bubbles, a potential at 10 mA cm^{-2} was held for 24 h at a rotation rate of 5000 rpm. It can be seen that even under these conditions, the CA curve features several spikes which originate from the formation/release of the oxygen microbubbles on/from the electrode surface. The microbubbles issue is well known in the OER community as it interferes with the evaluation of the intrinsic activity and stability of the catalysts [62,63]. However, despite the presence of the current spikes, the CA curve does not show a specific activity decay. To further investigate this, the LSV measurement was repeated after the stability test and is shown in Fig. 7b. The activity screening shows no discernible change, implying that the CCN–AO catalyst is completely stable in strongly alkaline media (1 M KOH). SEM, SEM–EDXS, and XPS were used to examine the catalyst that was subjected to the degradation protocol (Fig. 8). SEM analysis of the top surface morphology reveals no significant morphological changes, even though the surface roughness appears to be slightly larger. SEM-EDXS shows an increase in oxygen content and a decrease in Fe. This result is consistent with ICP-OES analysis of the KOH electrolyte, which showed that the concentrations of Fe increased over the 24-h stability test, but no Co or Ni were dissolved from the catalyst. The XPS spectra of the sample after the stability test are similar to those of the sample after the electrochemical activity test. The most intense Fe $2p_{3/2}$ peak is located at 711.4 eV, the Ni $2p_{3/2}$ peak is located at 855.4 eV, and the Co $2p_{3/2}$ peak is located at 780.4 eV. The oxide layer contains the oxidation states Fe (2+/3+), Ni(2+/3+), and Co(3+). The spectrum of Co $2p_{3/2}$ is

very similar to the one obtained before the stability test confirming the important role of the Co(3+) oxidation state in the catalyst performance. The excellent overall stability is due to the oxide structure and the strong film adhesion to the CCA substrate.

4. Conclusions

We demonstrated, for the first time, a facile two-step method combining nitridation and anodization steps for effective surface treatment of CCM. This synthesis route provides a novel and simple approach to CCM high surface area catalyst production, which cuts the need for complicated production routes and extensive instrumentation.

Using the introduced method, we produced compositionally complex high-surface-area electrocatalysts (FeCoNi–O) from bulk FeCoNiCuZn material, providing a hierarchical porous structure with optimized adhesion to the substrate. The obtained structures show excellent electrocatalytic performance towards OER in an alkaline solution. Moreover, measured overpotentials of the introduced system were found to be among the best reported for non-noble alkaline OER catalysts so far.

Due to the electrocatalytic performance, the enhanced stability of the catalytic performance and the wide applicability of experimental design, we emphasize the suitability of the introduced methods for industry applications. The energy-efficient anodization process provides a realistic way for the application of CCMs in electrocatalysis. Further optimization of the two-step synthesis method like fine-tuning of anodization parameters and variation of the material composition provide a promising path for future research in CCM catalyst design.

CRediT authorship contribution statement

Luka Suhadolnik: Conceptualization, Funding acquisition, Investigation, Methodology, Writing – original draft. **Marjan Bele:** Investigation, Methodology. **Milutin Smiljanić:** Investigation, Methodology, Writing – original draft. **Goran Dražić:** Investigation, Writing – original draft. **Lidija D. Rafailović:** Methodology, Writing – original draft. **Daniela Neumüller:** Investigation, Investigation, Writing – original draft. **Martin Šala:** Investigation, Writing – original draft. **Anja Lončar:** Data curation, Visualization. **Nejc Hodnik:** Funding acquisition, Writing – original draft. **Miran Gaberšček:** Formal analysis, and interpretation, Writing – original draft. **Janez Kovač:** Investigation, Writing – original draft. **Urška Trstenjak:** Investigation, Writing – original draft. **Tiziano Montini:** Investigation. **Michele Melchionna:** Methodology, Writing – original draft, Writing – review & editing. **Paolo Fornasiero:** Conceptualization, Funding acquisition, Supervision, Writing – review & editing.

Declaration of competing interest

The authors declare that they have no known competing financial interests or personal relationships that could have appeared to influence the work reported in this paper.

Data availability

Data will be made available on request.

Acknowledgments

L.S. acknowledges funding from the European Union's Horizon 2020 research and innovation programme under the Marie Skłodowska-Curie grant agreement No 101025516. N.H. acknowledges European Research Council (ERC) Starting Grant 123STABLE (Grant agreement ID: 852208). M. M. kindly acknowledges FRA 2022 funded by the University of Trieste. The provision of financial support for the research and the preparation of the manuscript by the Slovenian Research Agency (ARRS) within the research programs P2-0421, P1-0034, P2-0393, and P2-0082 and projects N2-0155, J2-3041, and N2-0248 is gratefully acknowledged. L. Rafailovic and D. Neumüller acknowledge support provided by University of Leoben. The authors also thank Edi Kranjc (Department of Inorganic Chemistry and Technology, National Institute of Chemistry, Slovenia) for the X-ray powder-diffraction measurements.

Appendix A. Supplementary data

Supplementary data to this article can be found online at https://doi.org/10.1016/j.mtchem.2023.101835.

References

[1] I. Katsounaros, S. Cherevko, A.R. Zeradjanin, K.J.J. Mayrhofer, Oxygen electrochemistry as a cornerstone for sustainable energy conversion, Angew. Chem. Int. Ed. 53 (2014) 102–121, https://doi.org/10.1002/anie.201306588.
[2] G. Glenk, S. Reichelstein, Economics of converting renewable power to hydrogen, Nat. Energy 4 (2019) 216–222, https://doi.org/10.1038/s41560-019-0326-1.
[3] J. Song, C. Wei, Z.F. Huang, C. Liu, L. Zeng, X. Wang, Z.J. Xu, A review on fundamentals for designing oxygen evolution electrocatalysts, Chem. Soc. Rev. 49 (2020) 2196–2214, https://doi.org/10.1039/C9CS00607A.
[4] P.P. Lopes, D.Y. Chung, X. Rui, H. Zheng, H. He, P.F.B.D. Martins, D. Strmcnik, V. R. Stamenkovic, P. Zapol, J.F. Mitchell, R.F. Klie, N.M. Markovic, Dynamically stable active sites from surface evolution of perovskite materials during the oxygen evolution reaction, J. Am. Chem. Soc. 143 (2021) 2741–2750, https://doi.org/10.1021/JACS.0C08959/SUPPL_FILE/JA0C08959_SI_001.PDF.
[5] D.Y. Chung, P.P. Lopes, P. Farinazzo Bergamo Dias Martins, H. He, T. Kawaguchi, P. Zapol, H. You, D. Tripkovic, D. Strmcnik, Y. Zhu, S. Seifert, S. Lee, V. R. Stamenkovic, N.M. Markovic, Dynamic stability of active sites in hydr(oxy) oxides for the oxygen evolution reaction, Nat. Energy 5 (2020) 222–230, https://doi.org/10.1038/s41560-020-0576-y, 2020 5:3.
[6] C. Oses, C. Toher, S. Curtarolo, High-entropy ceramics, Nat. Rev. Mater.. (n.d.). https://doi.org/10.1038/s41578-019-0170-8..
[7] B. Cantor, I.T.H. Chang, P. Knight, A.J.B. Vincent, Microstructural development in equiatomic multicomponent alloys, Mater. Sci. Eng. 375–377 (2004) 213–218, https://doi.org/10.1016/j.msea.2003.10.257.
[8] J.-W. Yeh, S.-K. Chen, S.-J. Lin, J.-Y. Gan, T.-S. Chin, T.-T. Shun, C.-H. Tsau, S.-Y. Chang, Nanostructured high-entropy alloys with multiple principal elements: novel alloy design concepts and outcomes, Adv. Eng. Mater. 6 (2004) 299–303, https://doi.org/10.1002/adem.200300567.
[9] B. Gludovatz, A. Hohenwarter, D. Catoor, E.H. Chang, E.P. George, R.O. Ritchie, A fracture-resistant high-entropy alloy for cryogenic applications, Science 345 (2014) 1153–1158, https://doi.org/10.1126/science.1254581, 1979.
[10] T.A.A. Batchelor, J.K. Pedersen, S.H. Winther, I.E. Castelli, K.W. Jacobsen, J. Rossmeisl, High-entropy alloys as a discovery platform for electrocatalysis, Joule 3 (2019) 834–845, https://doi.org/10.1016/j.joule.2018.12.015.
[11] T. Löffler, H. Meyer, A. Savan, P. Wilde, A. Garzón Manjón, Y.-T. Chen, E. Ventosa, C. Scheu, A. Ludwig, W. Schuhmann, Discovery of a multinary noble metal-free oxygen reduction catalyst, Adv. Energy Mater. 8 (2018), 1802269, https://doi.org/10.1002/aenm.201802269.
[12] F. Otto, Y. Yang, H. Bei, E.P. George, Relative effects of enthalpy and entropy on the phase stability of equiatomic high-entropy alloys, Acta Mater. 61 (2013) 2628–2638, https://doi.org/10.1016/J.ACTAMAT.2013.01.042.
[13] F. Otto, A. Dlouhý, C. Somsen, H. Bei, G. Eggeler, E.P. George, The influences of temperature and microstructure on the tensile properties of a CoCrFeMnNi high-entropy alloy, Acta Mater. 61 (2013) 5743–5755, https://doi.org/10.1016/J.ACTAMAT.2013.06.018.
[14] C. Feng, Z. Zhang, D. Wang, Y. Kong, J. Wei, R. Wang, P. Ma, H. Li, Z. Geng, M. Zuo, J. Bao, S. Zhou, J. Zeng, Tuning the electronic and steric interaction at the atomic interface for enhanced oxygen evolution, J. Am. Chem. Soc. 144 (2022) 9271–9279, https://doi.org/10.1021/JACS.2C00533/SUPPL_FILE/JA2C00533_SI_001.PDF.
[15] H.-J. Qiu, G. Fang, J. Gao, Y. Wen, J. Lv, H. Li, G. Xie, X. Liu, S. Sun, Noble metal-free nanoporous high-entropy alloys as highly efficient electrocatalysts for oxygen evolution reaction, ACS Mater. Lett. 1 (2019) 526–533, https://doi.org/10.1021/acsmaterialslett.9b00414.
[16] M.W. Glasscott, A.D. Pendergast, S. Goines, A.R. Bishop, A.T. Hoang, C. Renault, J. E. Dick, Electrosynthesis of high-entropy metallic glass nanoparticles for designer, multi-functional electrocatalysis, Nat. Commun. 10 (2019) 1–8, https://doi.org/10.1038/s41467-019-10303-z, 2019 10:1.
[17] F. Waag, Y. Li, A.R. Ziefuß, E. Bertin, M. Kamp, V. Duppel, G. Marzun, L. Kienle, S. Barcikowski, B. Gökce, Kinetically-controlled laser-synthesis of colloidal high-entropy alloy nanoparticles, RSC Adv. 9 (2019) 18547–18558, https://doi.org/10.1039/C9RA03254A.
[18] W. Dai, T. Lu, Y. Pan, Novel and promising electrocatalyst for oxygen evolution reaction based on MnFeCoNi high entropy alloy, J. Power Sources 430 (2019) 104–111, https://doi.org/10.1016/J.JPOWSOUR.2019.05.030.
[19] S.L. Fereja, Z. Zhang, Z. Fang, J. Guo, X. Zhang, K. Liu, Z. Li, W. Chen, High-entropy oxide derived from metal–organic framework as a bifunctional electrocatalyst for efficient urea oxidation and oxygen evolution reactions, ACS Appl. Mater. Interfaces (2022), https://doi.org/10.1021/ACSAMI.2C09161.

[20] M.V. Kante, M.L. Weber, S. Ni, I.C.G. van den Bosch, E. van der Minne, L. Heymann, L.J. Falling, N. Gauquelin, M. Tsvetanova, D.M. Cunha, G. Koster, F. Gunkel, S. Nemšák, H. Hahn, L. Velasco Estrada, C. Baeumer, A high-entropy oxide as high-activity electrocatalyst for water oxidation, ACS Nano 17 (2022) 5329–5339, https://doi.org/10.1021/ACSNANO.2C08096/ASSET/IMAGES/LARGE/NN2C08096_0006.JPEG.
[21] K.S.K.J. Reddy, L.P.P. Chokkakula, S.R. Dey, Strategies to engineer FeCoNiCuZn high entropy alloy composition through aqueous electrochemical deposition, Electrochim. Acta 453 (2023), 142350, https://doi.org/10.1016/J.ELECTACTA.2023.142350.
[22] B.R. Braeckman, F. Boydens, H. Hidalgo, P. Dutheil, M. Jullien, A.L. Thomann, D. Depla, High entropy alloy thin films deposited by magnetron sputtering of powder targets, Thin Solid Films 580 (2015) 71–76, https://doi.org/10.1016/J.TSF.2015.02.070.
[23] Z. An, H. Jia, Y. Wu, P.D. Rack, A.D. Patchen, Y. Liu, Y. Ren, N. Li, P.K. Liaw, Solid-solution CrCoCuFeNi high-entropy alloy thin films synthesized by sputter deposition, Mater Res Lett 3 (2015) 203–209, https://doi.org/10.1080/21663831.2015.1048904/SUPPL_FILE/TMRL_A_1048904_SM3737.DOC.
[24] S. Singh, M. Festin, W.R.T. Barden, L. Xi, J.T. Francis, P. Kruse, Universal method for the fabrication of detachable ultrathin films of several transition metal oxides, ACS Nano 2 (2008) 2363–2373, https://doi.org/10.1021/nn800488h.
[25] J.M. Macák, H. Tsuchiya, P. Schmuki, High-aspect-ratio TiO $_2$ nanotubes by anodization of titanium, Angew. Chem. Int. Ed. 44 (2005) 2100–2102, https://doi.org/10.1002/anie.200462459.
[26] Y. Kim, J. Jung, Preparation of nickel oxide films by anodizing, Korean Chem Eng Res 50 (2012) 204–210, https://doi.org/10.9713/kcer.2012.50.2.204.
[27] K. Xie, M. Guo, H. Huang, Y. Liu, Fabrication of iron oxide nanotube arrays by electrochemical anodization, Corrosion Sci. 88 (2014) 66–75, https://doi.org/10.1016/j.corsci.2014.07.019.
[28] M.J. M, T. Hiroaki, S. Patrik, High-aspect-ratio TiO2 nanotubes by anodization of titanium, Angew. Chem. Int. Ed. 44 (2005) 2100–2102, https://doi.org/10.1002/anie.200462459.
[29] C.-Y. Lee, K. Lee, P. Schmuki, Anodic Formation of self-organized cobalt oxide nanoporous layers, Angew. Chem. Int. Ed. 52 (2013) 2077–2081, https://doi.org/10.1002/anie.201208793.
[30] X. Shu, H. Zheng, G. Xu, J. Zhao, L. Cui, J. Cui, Y. Qin, Y. Wang, Y. Zhang, Y. Wu, The anodization synthesis of copper oxide nanosheet arrays and their photoelectrochemical properties, Appl. Surf. Sci. 412 (2017) 505–516, https://doi.org/10.1016/J.APSUSC.2017.03.267.
[31] J. Dong, Z. Liu, J. Dong, D. Ariyanti, Z. Niu, S. Huang, W. Zhang, W. Gao, Self-organized ZnO nanorods prepared by anodization of zinc in NaOH electrolyte, RSC Adv. 6 (2016) 72968–72974, https://doi.org/10.1039/C6RA16995C.
[32] H. Wu, C. Feng, L. Zhang, J. Zhang, D.P. Wilkinson, Non-noble metal electrocatalysts for the hydrogen evolution reaction in water electrolysis, Electrochem. Energy Rev. 4 (2021) 473–507, https://doi.org/10.1007/S41918-020-00086-Z, 2021 4:3.
[33] L. Qin, Q. Chen, R. Lan, R. Jiang, X. Quan, B. Xu, F. Zhang, Y. Jia, Effect of anodization parameters on morphology and photocatalysis properties of TiO2 nanotube arrays, J. Mater. Sci. Technol. 31 (2015) 1059–1064, https://doi.org/10.1016/j.jmst.2015.07.012.
[34] L. Wang, T.T. Zhao, Z. Zhang, G. Li, Fabrication of highly ordered TiO 2 nanotube arrays via anodization of Ti-6AI-4V alloy sheet, J. Nanosci. Nanotechnol. 10 (2010) 8312–8321, https://doi.org/10.1166/jnn.2010.3006.
[35] L. Li, J. Wu, L. Huang, G. Lan, N. Wang, H. Zhang, X. Chen, X. Ge, In situ generation of Ni/Fe hydroxide layers by anodic etching of a Ni/Fe film for efficient oxygen evolution reaction, New J. Chem. (2022), https://doi.org/10.1039/D1NJ05775H.
[36] L. Suhadolnik, M. Bele, M. Čekada, P. Jovanovič, N. Maselj, A. Lončar, G. Dražić, M. Šala, N. Hodnik, J. Kovač, T. Montini, M. Melchionna, P. Fornasiero, Nanotubular TiOxNy-supported Ir single atoms and clusters as thin-film electrocatalysts for oxygen evolution in acid media, Chem. Mater. 35 (2023) 2612–2623, https://doi.org/10.1021/ACS.CHEMMATER.3C00125/ASSET/IMAGES/LARGE/CM3C00125_0006.JPEG.
[37] Kabekkodu, PDF-4+, 2021.
[38] D. Nečas, P. Klapetek, Gwyddion: an open-source software for SPM data analysis, Cent. Eur. J. Phys. 10 (2012) 181–188, https://doi.org/10.2478/S11534-011-0096-2/MACHINEREADABLECITATION/RIS.
[39] W. Gierlotka, S.W. Chen, Thermodynamic descriptions of the Cu-Zn system, J. Mater. Res. 23 (2008) 258–263, https://doi.org/10.1557/JMR.2008.0035/FIGURES/6.
[40] H. hui Liu, H. ling Zhang, H. bin Xu, T. ping Lou, Z. tong Sui, Y. Zhang, Hierarchically nanostructured vanadium nitride microspheres assembled with porous nanosheets fabricated by a template-free route, Ceram. Int. 44 (2018) 1583–1588, https://doi.org/10.1016/J.CERAMINT.2017.10.078.
[41] J.S. Kang, J. Kim, J.S. Kim, K. Nam, H. Jo, Y.J. Son, J. Kang, J. Jeong, H. Choe, T. H. Kwon, Y.E. Sung, Electrochemically synthesized mesoscopic nickel oxide films as photocathodes for dye-sensitized solar cells, ACS Appl. Energy Mater. 1 (2018) 4178–4185, https://doi.org/10.1021/ACSAEM.8B00834/SUPPL_FILE/AE8B00834_SI_001.PDF.
[42] W.J. Stępniowski, D. Paliwoda, Z. Chen, K. Landskron, W.Z. Misiołek, Hard anodization of copper in potassium carbonate aqueous solution, Mater. Lett. 252 (2019) 182–185, https://doi.org/10.1016/J.MATLET.2019.05.126.
[43] D. Gizí Nski, A. Brudzisz, M. Ramadan Alzahrani, K.-K. Wang, W.Z. Misiołek, W. J. St Epniowski, G. Nski, D. Brudzisz, A. Alzahrani, M.R. Wang, K.-K. Misiołek, W. Z. St, K. Syrek, Formation of CuOx nanowires by anodizing in sodium bicarbonate solution, Crystals 11 (2021) 624, https://doi.org/10.3390/CRYST11060624, 11 (2021) 624.
[44] D.T. Sorensen, A.W. Davidson, J. Kleinberg, The anodic oxidation of zinc and cadmium in aqueous solution, J. Inorg. Nucl. Chem. 13 (1960) 64–72, https://doi.org/10.1016/0022-1902(60)80237-0.
[45] L. Zaraska, K. Mika, K. Syrek, G.D. Sulka, Formation of ZnO nanowires during anodic oxidation of zinc in bicarbonate electrolytes, J. Electroanal. Chem. 801 (2017) 511–520, https://doi.org/10.1016/J.JELECHEM.2017.08.035.
[46] K. Engelkemeier, A. Sun, D. Voswinkel, O. Grydin, M. Schaper, W. Bremser, Zinc anodizing: structural diversity of anodic zinc oxide controlled by the type of electrolyte, Chemelectrochem 8 (2021) 2155–2168, https://doi.org/10.1002/CELC.202100216.
[47] W.Y. An, H. Lee, S.R. Choi, S. Choi, H.-S. Cho, M. Choi, J.-Y. Park, Hierarchically porous Ni foam-supported Co and Sn doped Ni3S2 nanosheets for oxygen evolution reaction electrocatalysts, J Mater Chem A Mater 11 (2023) 5734–5745, https://doi.org/10.1039/D2TA09361H.
[48] G. Hyun, J.T. Song, C. Ahn, Y. Ham, D. Cho, J. Oh, S. Jeon, Hierarchically porous Au nanostructures with interconnected channels for efficient mass transport in electrocatalytic CO2 reduction, Proc. Natl. Acad. Sci. U. S. A. 117 (2020) 5680–5685, https://doi.org/10.1073/PNAS.1918837117/SUPPL_FILE/PNAS.1918837117.SAPP.PDF.
[49] S. Cherevko, X. Xing, C.H. Chung, Electrodeposition of three-dimensional porous silver foams, Electrochem. Commun. 12 (2010) 467–470, https://doi.org/10.1016/J.ELECOM.2010.01.021.
[50] Y. Qiu, L. Xin, W. Li, Electrocatalytic oxygen evolution over supported small amorphous ni-fe nanoparticles in alkaline electrolyte, Langmuir 30 (2014) 7893–7901, https://doi.org/10.1021/LA501246E/ASSET/IMAGES/LARGE/LA-2014-01246E_0007.JPEG.
[51] R. Pinsky, P. Sabharwall, J. Hartvigsen, J. O'Brien, Comparative review of hydrogen production technologies for nuclear hybrid energy systems, Prog. Nucl. Energy 123 (2020), 103317, https://doi.org/10.1016/J.PNUCENE.2020.103317.
[52] B. Zhang, X. Zheng, O. Voznyy, R. Comin, M. Bajdich, M. García-Melchor, L. Han, J. Xu, M. Liu, L. Zheng, F.P.G. De Arquer, C.T. Dinh, F. Fan, M. Yuan, E. Yassitepe, N. Chen, T. Regier, P. Liu, Y. Li, P. De Luna, A. Janmohamed, H.L. Xin, H. Yang, A. Vojvodic, E.H. Sargent, Homogeneously dispersed multimetal oxygen-evolving catalysts, Science 352 (2016) 333–337, https://doi.org/10.1126/SCIENCE.AAF1525/SUPPL_FILE/ZHANG-SM.PDF, 1979.
[53] P. He, X.Y. Yu, X.W.D. Lou, Carbon-incorporated nickel–cobalt mixed metal phosphide nanoboxes with enhanced electrocatalytic activity for oxygen evolution, Angew. Chem. Int. Ed. 56 (2017) 3897–3900, https://doi.org/10.1002/ANIE.201612635.
[54] X. Zhao, Z. Xue, W. Chen, X. Bai, R. Shi, T. Mu, Ambient fast, large-scale synthesis of entropy-stabilized metal–organic framework nanosheets for electrocatalytic oxygen evolution, J Mater Chem A Mater 7 (2019) 26238–26242, https://doi.org/10.1039/C9TA09975A.
[55] A. Lončar, P. Jovanovič, N. Hodnik, M. Gaberšček, Determination of the electroactive surface area of supported Ir-based oxygen evolution catalysts by impedance spectroscopy: observed anomalies with respect to catalyst loading, J. Electrochem. Soc. 170 (2023), 044504, https://doi.org/10.1149/1945-7111/ACCAAD.
[56] S. Watzele, P. Hauenstein, Y. Liang, S. Xue, J. Fichtner, B. Garlyyev, D. Scieszka, F. Claudel, F. Maillard, A.S. Bandarenka, Determination of electroactive surface area of Ni-, Co-, Fe-, and Ir-based oxide electrocatalysts, ACS Catal. 9 (2019) 9222–9230, https://doi.org/10.1021/ACSCATAL.9B02006/SUPPL_FILE/CS9B02006_SI_001.PDF.
[57] L. Song, S. Zhu, L. Tong, W. Wang, C. Ouyang, F. Xu, Y. Wang, MXene quantum dot rivet reinforced Ni–Co LDH for boosting electrochemical activity and cycling stability, Mater Adv 2 (2021) 5622–5628, https://doi.org/10.1039/D1MA00474C.
[58] T.H.T. Nguyen, Z. Zarkua, C.V. Chinnappa, W. Hu, S.P. Sree, D. Grandjean, D. Pant, E. Janssens, Co3−xFexO4 inverse opals with tunable catalytic activity for high-performance overall water splitting, Nanoscale 15 (2023) 10306–10318, https://doi.org/10.1039/D2NR07300E.
[59] Y. Bi, Z. Cai, D. Zhou, Y. Tian, Q. Zhang, Q. Zhang, Y. Kuang, Y. Li, X. Sun, X. Duan, Understanding the incorporating effect of Co2+/Co3+ in NiFe-layered double hydroxide for electrocatalytic oxygen evolution reaction, J. Catal. 358 (2018) 100–107, https://doi.org/10.1016/J.JCAT.2017.11.028.
[60] C.B. Mullins, Y.J. Son, K. Kawashima, B.R. Wygant, C.H. Lam, J.N. Burrow, H. Celio, A. Dolocan, J.G. Ekerdt, Anodized nickel foam for oxygen evolution reaction in fe-free and unpurified alkaline electrolytes at high current densities, ACS Nano 15 (2021) 3468–3480, https://doi.org/10.1021/ACSNANO.0C10788/ASSET/IMAGES/MEDIUM/NN0C10788_M010.GIF.
[61] R.A. Márquez, K. Kawashima, Y.J. Son, G. Castelino, N. Miller, L.A. Smith, C. E. Chukwuneke, C.B. Mullins, Getting the basics right: preparing alkaline electrolytes for electrochemical applications, ACS Energy Lett. 8 (2023) 1141–1146, https://doi.org/10.1021/ACSENERGYLETT.2C02847/ASSET/IMAGES/LARGE/NZ2C02847_0003.JPEG.
[62] H.A. El-Sayed, A. Weiß, L.F. Olbrich, G.P. Putro, H.A. Gasteiger, OER catalyst stability investigation using RDE technique: a stability measure or an artifact? J. Electrochem. Soc. 166 (2019) F458–F464, https://doi.org/10.1149/2.0301908jes.
[63] A. Hartig-Weiss, M.F. Tovini, H.A. Gasteiger, H.A. El-Sayed, OEr catalyst durability tests using the rotating disk electrode technique: the reason why this leads to erroneous conclusions, ACS Appl. Energy Mater. 3 (2020) 10323–10327, https://doi.org/10.1021/ACSAEM.0C01944/ASSET/IMAGES/MEDIUM/AE0C01944_0003.GIF.